Evaluation of selected Fe–Cr steels under single- and dual-atmosphere conditions for intermediate-temperature solid oxide fuel cell interconnect

International Journal of Hydrogen Energy 65 (2024) 112–125

Contents lists available at ScienceDirect

International Journal of Hydrogen Energy

journal homepage: www.elsevier.com/locate/he

Evaluation of selected Fe–Cr steels under single- and dual-atmosphere conditions for intermediate-temperature solid oxide fuel cell interconnect applications

Matthieu Tomas *, Jan-Erik Svensson, Jan Froitzheim

Department of Chemistry and Chemical Engineering, Chalmers University of Technology, Kemivägen 10, 41296, Gothenburg, Sweden

ARTICLE INFO

Handling Editor: Fanglin F. Chen

Keywords:
IT-SOFC
Interconnect
Cr(VI) evaporation
Dual-atmosphere
Corrosion
Laves phases

ABSTRACT

For Intermediate-Temperature SOFC, the lower operating temperature allows for a broader range of steel grades to be used as interconnects. This work compares the oxidation performances of six Cr_2O_3-forming steels and one Al_2O_3-forming steel, under single- and dual-atmosphere conditions.

Single-atmosphere exposures in combination with Cr(VI) evaporation measurements were carried out at 600 °C. Except for AISI 430 all the Cr_2O_3-forming steels showed protective behaviour with similar Cr(VI) evaporation values and low area specific resistance (ASR) values. Kanthal EF101 showed the lowest level of Cr (VI) vaporisation but substantially higher ASR values.

Dual-atmosphere exposures were carried out at 600 °C in Ar-5%H_2–3%H_2O//air-3%H_2O. All Cr_2O_3-forming steels suffered various degrees of breakaway corrosion. Therefore, operation under dual-atmosphere conditions is likely the life-time-limiting failure mode.

1. Introduction

Traditional SOFC designs have used lanthanum chromite-based interconnects. However, due to their high cost, they have been replaced with high-steel, low-volume special steels such as Crofer 22 APU. This approach has proven successful for operating temperatures of around 800 °C. Recent developments in relation to Solid Oxide Fuel Cell (SOFC) systems have allowed for lower operating temperatures (500°–750 °C), paving the way for a broader range of materials and cheaper fabrication, particularly in terms of the interconnects. The lower operating temperature allows for faster start-up and shut-down, potentially giving lower corrosion rates and improved durability of the metallic components [1]. Intermediate-Temperature SOFCs (IT-SOFCs) utilise either very thin electrolytes thereby reducing the area-specific resistance (ASR), or alternative materials with higher ionic conductivity, such as gadolinium-doped ceria [2].

Ferritic stainless steels are currently the most commonly used interconnect materials. The most-important parameters to consider regarding interconnects are: the material stability when exposed to high temperature; and the electrical resistance of the formed oxide. When exposed to high temperatures, ferritic stainless steels form a Cr_2O_3 scale that represents a good compromise between corrosion resistance and electronic conductivity. However, those materials suffer from Cr(VI) evaporation. The evaporated Cr(VI) will eventually be deposited onto the cathode, significantly reducing its catalytic properties [3]. The materials used in SOFC interconnects are alloyed with manganese (Mn). When oxidised, Mn-containing ferritic stainless steels have been shown to form a (Cr, Mn)$_3O_4$ spinel layer on top of a chromia scale, in the temperature range of the SOFC [4–6]. The presence of a (Cr, Mn)$_3O_4$ reduces Cr(VI) evaporation, however it is still significant.

Since Cr_2O_3 is a relatively poor electrical conductor, Cr_2O_3 scale growth over time has a direct impact on stack degradation, so Cr_2O_3 scale growth should be limited. Hou et al. [7] have described the beneficial effects of reactive elements (REs) on Cr_2O_3-forming steels through the selective oxidation of Cr, reducing the Cr_2O_3 scale growth rate or changing the transport mechanism from outward metal transport to inward oxygen diffusion. Compared to samples that lack an RE layer, a clear difference in chromia thickness has been observed for samples that are coated with a thin ceria layer [8].

Another noticeable corrosion phenomenon is the so-called *Dual-atmosphere effect*. When exposed to two different atmospheres, i.e., humid air on the cathode side and hydrogen on the anode side, increased corrosion is observed on the air-side of the interconnect [9–13]. The severity of the dual-atmosphere effect differs between studies. At high

* Corresponding author.
E-mail address: tommat@chalmers.se (M. Tomas).

https://doi.org/10.1016/j.ijhydene.2024.04.010
Received 25 January 2024; Received in revised form 28 March 2024; Accepted 1 April 2024
Available online 4 April 2024

Table 1
Batch specific compositions of the studied steels (in wt%), as specified by the manufacturer.

Materials	Fe	Cr	C	Mn	Si	Ni	Ti	Nb	Al	Cu	La	Mo	W
Crofer 22 APU *(EN 1.4760)*	*Bal.*	**22.92**	0.004	0.38	0.01	/	0.06	/	/	0.01	**0.09**	/	/
Crofer 22 H *(EN 1.4755)*	*Bal.*	**22.61**	0.018	0.42	0.35	0.46	0.09	**0.49**	0.02	0.02	**0.07**	/	**1.94**
AISI 441 *(EN 1.4509)*	*Bal.*	**17.53**	0.016	0.40	0.59	0.15	0.172	0.41	0.007	/	/	/	/
EN 1.4622 *(EN 1.4622)*	*Bal.*	**20.8**	0.019	0.38	0.45	0.2	0.173	0.25	/	**0.38**	/	/	/
AISI 444 *(EN 1.4521)*	*Bal.*	**19.03**	0.015	0.35	0.40	0.18	0.005	**0.60**	0.002	0.092	/	**1.86**	/
AISI 430 *(EN 1.4016)*	*Bal.*	**16.20**	0.040	0.49	0.34	/	/	/	/	/	/	/	/
Kanthal EF 101	*Bal.*	**12.4**	0.02	0.10	1.25	/	/	/	**3.7**	/	/	/	/

Table 2
Compositions of the different batches of Crofer 22 APU and Crofer 22 H (in wt%), as specified by the manufacturer. Batch A refers to the material compositions described in Table I.

Materials	Fe	Cr	C	Mn	Si	Ni	Ti	Nb	Cu	La	W
Crofer 22 APU *(Batch A)*	*Bal.*	**22.92**	0.004	0.38	0.01	/	0.06	/	0.01	**0.09**	/
Crofer 22 APU *(Batch B)*	*Bal.*	**22.8**	0.004	0.4	0.02	/	0.06	/	0.01	**0.1**	/
Crofer 22 APU *(Batch C)*	*Bal.*	**22.74**	0.002	0.45	0.02	0.01	0.06	<0.01	/	/	/
Crofer 22 H *(Batch A)*	*Bal.*	**22.61**	0.018	0.42	**0.35**	0.46	0.09	**0.49**	0.02	**0.07**	**1.94**
Crofer 22 H *(Batch B)*	*Bal.*	**22.93**	0.008	0.46	**0.22**	0.26	0.06	**0.5**	0.02	**0.07**	**2.12**
Crofer 22 H *(Batch C)*	*Bal.*	**22.56**	0.009	0.43	**0.24**	/	0.06	**0.49**	0.02	**0.05**	**1.97**

temperatures (800° – 850 °C), several authors [14–16] have observed an enrichment of Fe in the scale on the air-side. At lower temperatures (~600 °C), the interconnect undergoes severe corrosion with the formation of hematite nodules and subsequent formation of a thick hematite scale [13,17,18]. This phenomenon leads to a fast-growing, non-protective iron oxide scale, which reduces the performance of the interconnect.

Several explanations have been put forward to explain this mechanism. *Rufner* et al. [19] have suggested that the partial pressure of oxygen (pO_2) on the air-side is locally modified by the permeating hydrogen. In contrast, *Yang* et al. [15] have suggested an increased concentration of cation vacancies in the oxide, which increases the growth rate of the scale. In a recent study, *Gunduz* et al. [13] have proposed that hydrogen does not affect oxygen permeability, and that there is no direct effect of hydrogen on the growth of the oxide scale. Instead, they have proposed that hydrogen causes the breakdown of the protective Cr_2O_3 scale due to a reduction of Cr transport along the metal grain boundaries.

Previous work [20–23] found improved corrosion resistance after pre-oxidation of ferritic stainless steels. *Goebel* et al. [24] studied this effect and found a clear correlation between pre-oxidation duration and resistance towards dual-atmosphere induced breakaway corrosion. The beneficial effect of pre-oxidation has been attributed to the barrier properties of the fuel-side Cr_2O_3 layer. This is in line with data by *Kurokawa* et al. [25] that demonstrated a reduction of hydrogen permeation by four orders of magnitude at 800 °C through the presence of chromia. However, it is important to note that pre-oxidation does not appear to provide a long-term solution to the challenges associated with dual-atmosphere corrosion, as indicated by previous research [13,26,27]. The present paper investigates different commercial steels for IT-SOFC interconnect applications, including Crofer 22 APU, Crofer 22H, AISI 441, EN 1.4622, AISI 444, AISI 430 and Kanthal EF 101. The steels were exposed to single- and dual-atmosphere conditions for 3 weeks to evaluate the effects of alloying elements on the oxidation properties. Separate samples were exposed in a single-atmosphere environment to measure the Cr(VI) evaporation and the mass gain.

2. Materials and methods

Six commercial Cr_2O_3-forming steels and one alumina-forming steel were selected for this comparative study. Their compositions (in wt%) are presented in Table I. Crofer 22 APU (ThyssenKrupp VDM) has a very low Si content. Crofer 22 H, AISI 441 and AISI 444 are Laves phase-forming steels due to additions of niobium [28], partly in combination with tungsten (W) or molybdenum (Mo). EN 1.4622 contains some Nb and also Cu, possibly to reduce further the Cr(VI) evaporation [29]. AISI 430, Kanthal EF101 and Crofer 22 APU do not from any Laves phases. Kanthal EF 101 has 3.7 wt% Al, and over time forms a thin protective Al_2O_3 scale, which has good corrosion properties.

Table 3
Average grain sizes of the studied Cr_2O_3-forming steels after exposure to dual-atmosphere conditions (Ar-5% H_2 + 3% H_2O//Air + 3% H_2O) for 500 h at 600 °C. Measurements are based on the intersects method described in the ASTM E112.

Studied steel	Average grain size (μm)
Crofer 22 APU *(EN 1.4760)*	18
Crofer 22 H *(EN 1.4755)*	32
AISI 441 *(EN 1.4509)*	21
EN 1.4622 (EN 1.4622)	18
AISI 444 *(EN 1.4521)*	24
AISI 430 *(EN 1.4016)*	9

For Crofer 22 APU and Crofer 22 H, three different batches were compared in greater detail. The batches are specified in Table II. Table III provides estimates of the grain sizes of the different steels. Most of the materials have an average grain size of approximately 20 μm, with AISI 430 having substantially smaller grains and Crofer 22 H having substantially larger grains.

Square-shaped samples (15 mm × 15 mm) were cut out of a metal sheet (0.3 mm in thickness) for the single-atmosphere exposures. The samples were cleaned with acetone for 20 min and with ethanol for 20 min in an ultrasonic bath before any thermal treatment. Except for AISI 430 which was tested in as-received and pre-oxidised condition all the single atmosphere experiments were carried out on non-pre-oxidised as-received samples.

For the dual-atmosphere exposures, coin-shaped samples (Ø 21 mm) were stamped out of a metal sheet using a hydraulic press. The samples were ground to a thickness of 0.2 mm using the Struers RotoPol-31, and then polished to 0.25 μm with a diamond paste using the Struers TegraPol-31 polisher grinder. A cleaning procedure that consisted of washing for 20 min in acetone and 20 min in ethanol was performed before any thermal treatment. All the samples were then pre-oxidised at 800 °C ± 5 °C for 20 min in air +3% H_2O, under a flow of 280 mL min^{-1}. The reason for pre-oxidation was that earlier work [13,20–24] has shown that non-pre-oxidised materials show severe breakaway corrosion and no differentiation between materials would have been possible.

Pre-oxidation also serves the purpose of mimicking the sealing process during stack manufacturing.

The method used for grain size measurement is based on the intersect method described in ASTM E112. However, higher magnification SEM micrographs were used, therefore less intersections were available, and the results are less accurate.

2.1. Cr(VI) evaporation and gravimetric measurements

Single-atmosphere exposures (for Cr(VI) evaporation and gravimetric measurements) were carried out in horizontal tube furnaces using an air-flow of 6000 s min^{-1} and 3% humidity for up to 500 h. To adjust the humidity level to 3%, all the gases were bubbled through water baths with temperature-controlled reflux condensers set at 24.4 °C. Cr(VI) vaporisation is a significant issue in terms of the longevity of the FC stack. Therefore, it is necessary to quantify the rate of Cr(VI) evaporation during the exposure. Cr(VI) vaporisation was measured for all samples using the denuder technique, which allows in situ determinations of Cr(VI) evaporation. A detailed description of the Cr(VI) evaporation measurement procedure can be found elsewhere [30]. At least two sets with three samples for each steel were exposed, as-received, in a tubular furnace for 500 h to ensure reproducibility, and Cr(VI) evaporation measurements were performed at regular intervals.

In this work, the net mass gain and the gross mass gain were evaluated. The gross mass gain corresponds to the net mass gain (weight after exposure) corrected for the mass loss due to Cr(VI) evaporation (measured throughout the exposure). In a humid atmosphere, the predominant volatile species of Cr is $CrO_2(OH)_2$ [see Eq. (1)] [31,32]:

$$Cr_2O_3(s) + 2H_2O\ (g) + 1.5O_2\ (g) \rightarrow 2CrO_2(OH)_2\ (g) \quad (1)$$

Equation (1) allows linkage of the loss of Cr_2O_3 from the scale to the volatilisation of Cr via the formation of $CrO_2(OH)_2$. Thus, each milligram (mg) of Cr(VI) lost from the oxide scale results in an equivalent loss of 1.46 mg of Cr_2O_3 [32].

2.2. Area-specific resistance measurements

The ASR is the measured resistance (R) multiplied by the contact area (A). A sputter mask with an opening of 10 × 10 mm^2 was placed on the sample, which was then coated with gold for 2 min using the Quorum 150 sputter coater and a sputtering current of 60 mA. This procedure was repeated for the reverse side of the sample. The sputtering step was used to produce electrodes with a defined area. The sputtered area was then painted with Metalor M − 9875 gold paint. Sintering of the gold paint was achieved in a two-step process: a drying step for 10 min at 150 °C; and a sintering step for 2 h at 600 °C. This ensured good contact between the sample and the platinum electrodes. The exposed samples were then mounted in a ProboStat™ (NorECs, Norway) measurement set-up using a 1-cm^2 platinum wire and grid to contact the sample electrodes and a Keithley 2400 source meter. The applied current was set to 100 mA cm^{-2}. The resistance was measured by the 2-point, 4-wire method at 600 °C in Ar – 5% H_2 + 3% H_2O for 1 h. During the subsequent cooling of the sample, the ASR was monitored to check for semi-conductive behaviour.

2.3. Dual-atmosphere exposures

All the dual-atmosphere experiments were conducted using the experimental set-up described by *Alnegren* et al. [9]. The sample holder construction is based on a design created by Montana State University, and further information on this set-up can be found elsewhere [19]. Gold rings were used to seal the circular samples to the set-up, to ensure gas-tightness. For the dual atmosphere experiments the coin-shaped samples were pre-oxidised at 800 °C for 20 min and subsequently exposed to a humid dual-atmosphere at 600 °C. The reason for pre-oxidation was that earlier work [13,24] has shown that non-pre-oxidised materials show severe breakaway corrosion and no differentiation between materials would have been possible. The following conditions were used: Ar–5 % H_2 + 3% H_2O at a flow rate of 120 smL•min^{-1} on the fuel-side; and air +3% H_2O at a flow rate of 8800 smL•min^{-1} on the air-side. To adjust the humidity level to 3%, all the gases were bubbled through water baths with temperature-controlled reflux condensers set at 24.4 °C. All exposures were conducted at a temperature of 600 °C ± 5 °C. The exposure was interrupted after 500 h. All dual-atmosphere experiments were repeated to ensure data reproducibility.

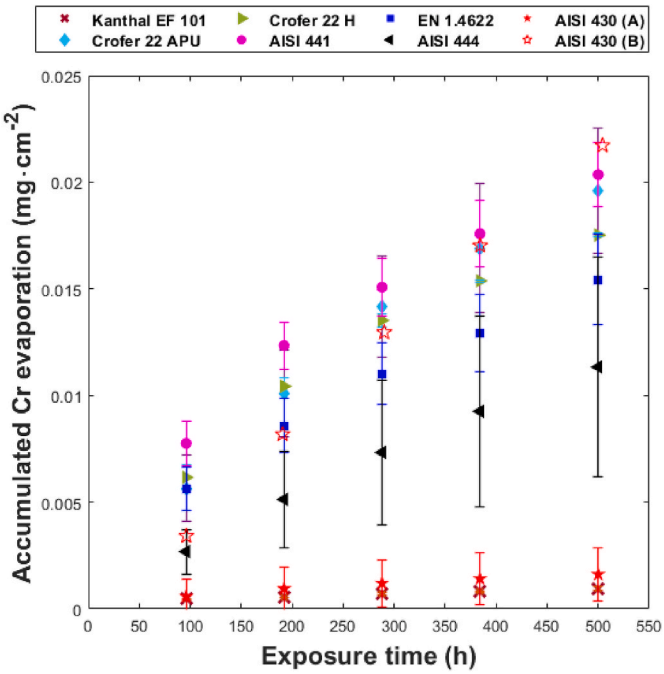

Fig. 1. Cumulative Cr(VI) evaporation levels as a function of time for AISI 441 (magenta circles), EN 1.4622 (dark-blue squares), Crofer 22 APU (Batch A) (cyan diamonds), Crofer 22 H (Batch A) (green triangles), AISI 444 (black arrow-head), AISI 430 (A) (filled red pentagon), AISI 430 pre-oxidised (B) (empty red pentagon), Kanthal EF 101 (brown cross), all of which were exposed at 600 °C in air that contained 3% water vapour. The error bars represent the standard deviation. (For interpretation of the references to colour in this figure legend, the reader is referred to the Web version of this article.)

2.4. Analysis

Photographs of the samples were taken at different exposure times using a Nikon SMZ800 camera equipped with a ring light. For the cross-sectional analyses, the samples were cut with an oil-free, low-speed saw (Struers Minitom). Cross-sections of all the samples were then prepared using a Leica EM TIC 3X Broad Ion Beam [33] milling instrument with an acceleration voltage of 8 kV and a current of 3 mA. The resulting cross-sections were analysed using the JEOL 7800F Prime scanning electron microscope (SEM). Imaging was performed with an acceleration voltage of 10 kV, and energy-dispersive x-ray (EDX) analysis was performed with an acceleration voltage of 15 kV. XRD analysis was performed using an XRD - Bruker D8 Discover mounted with $Cu_{K\alpha}$ radiation (λ = 1.5406 Å).

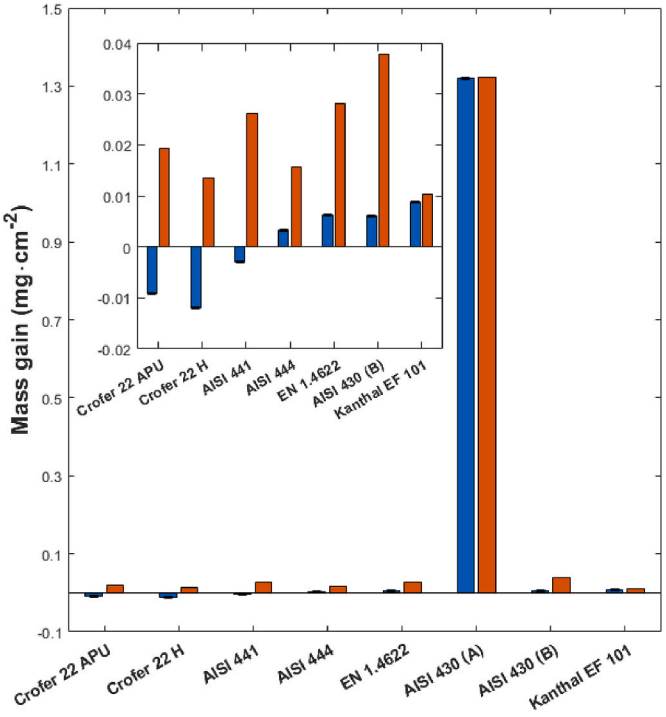

Fig. 2. The left bar (blue) represents the **net average mass gain**, and the right bar (orange) represents the **gross average mass gain** of the different steels exposed for 500 h at 600 °C in air that contained 3% water vapour. Batch A was used for Crofer 22 APU and Crofer 22 H. The error bars represent the standard deviations of the net mass gains. (For interpretation of the references to colour in this figure legend, the reader is referred to the Web version of this article.)

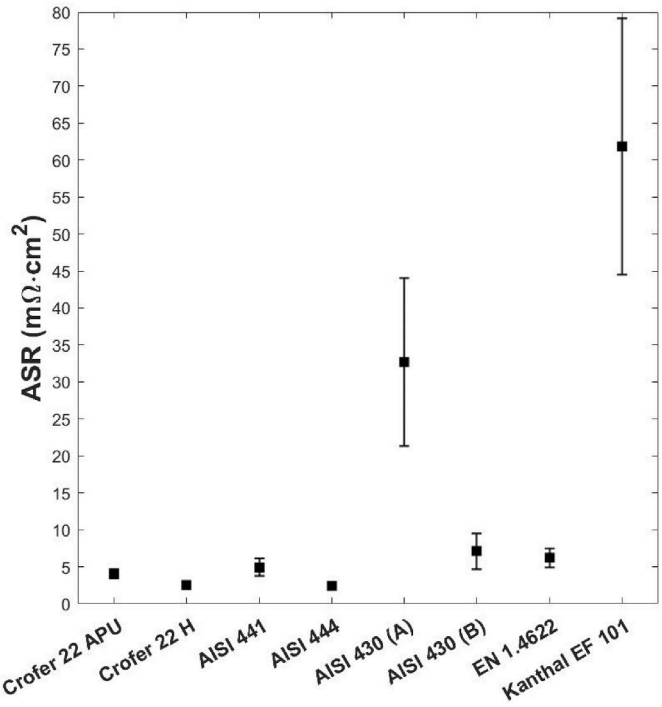

Fig. 3. ASR measurements in air at 600 °C, on different uncoated ferritic stainless steels after exposure at 600 °C for 500 h in air +3% H_2O. Error bars indicate standard deviation.

3. Results

3.1. (Single-atmosphere experiments)

3.1.1. Cr(VI) evaporation

The cumulative Cr(VI) evaporation levels for all the steels exposed at 600 °C are plotted as a function of time in Fig. 1. The Cr_2O_3-forming steels display approximately similar levels of Cr(VI) evaporation, with a mean of 0.017 ± 0.005 mg cm^{-2} after 500 h of exposure at 600 °C. However, AISI 430 displays two different behaviours: Behaviour A (as-received); and Behaviour B (pre-oxidised). AISI 430 (A) has a 10-fold lower level of Cr(VI) evaporation, of approximately 0.0018 mg cm^{-2} after 500 h, compared to the other Cr_2O_3-forming steels. This low value is attributed to breakaway oxidation leading to the formation of Fe oxide (see Fig. 5). Another set of AISI 430 [AISI 430 (B)] was pre-oxidised for 20 min at 800 °C, so as to form a protective Cr_2O_3 scale and avoid breakaway oxidation. These samples show a much higher level of Cr(VI) evaporation (~0.021 mg cm^{-2}) after 500 h of exposure. Kanthal EF 101 exhibits the lowest Cr(VI) evaporation, at approximately 0.00095 mg cm^{-2} after 500 h of exposure. FeCrAl steels are known to form transient alumina layers at lower temperatures [34,35]. The thin Al-rich layer formed during exposure drastically reduced the level of Cr(VI) evaporation, as compared to the chromia-forming steels.

3.1.2. Gravimetric measurements

Fig. 2 presents the average net and gross mass gains of the different steels after 500 h of exposure at 600 °C in air +3% H_2O. Crofer 22 APU, Crofer 22 H and AISI 441 show negative net mass gains. However, once compensation is made for the mass loss caused by the Cr(VI) evaporation, these three steels show positive gross mass gains of 0.019 mg cm^{-2}, 0.013 mg cm^{-2} and 0.027 mg cm^{-2}, respectively. EN 1.4622 and AISI 444 exhibit weakly positive net mass gains after exposure and gross mass gains of approximately 0.028 mg cm^{-2} and 0.016 mg cm^{-2}, respectively.

The net mass gain for AISI 430 (A = as-received) is representative of the breakaway oxidation that happened during the exposure (see Fig. 5), which means that there is a high mass gain of approximately 1.3 mg cm^{-2} after 500 h of exposure. The gross mass gain is similar to the net mass gain due to the low level of Cr(VI) evaporation. The net mass gain for AISI 430 (B = pre-oxidised) is much lower than that for AISI 430 (A), indicating that no breakaway oxidation occurred in the former. Kanthal EF 101 exhibits a net mass gain of about 0.009 mg cm^{-2} after 500 h, corresponding to the initial growth of the transient oxide layer followed by slow growth of the aluminium oxide.

3.1.3. Area-specific resistance measurements

Fig. 3 shows the ASR measurements performed in air on the different steel grades studied in this work. Apart from AISI 430 (A), which showed significant breakaway oxidation, all the Cr_2O_3-forming steels exhibit low ASR values of approximately 6 mΩ cm^2 on average. This matches well with previous results of *Falk Windisch* et al. [36] measured an ASR value of approximately 4 mΩ cm^2 on Sanergy HT exposed at 650 °C for 500h. Additionally, these results indicate a similar thickness of the Cr_2O_3 layer for all the Cr_2O_3-forming steels. The higher ASR values for AISI 430 (A) is attributed to a higher thickness of a non-protective Fe-rich oxide scale due to breakaway oxidation, which is in line with the high mass gain observed (see Fig. 2). The large variation observed for AISI 430 (A) is attributed to the different extend of breakaway oxidation on each sample, influencing the overall thickness and contact area. Kanthal EF 101 displays the highest ASR values. This is expected because of the growth of a thin transient Al_2O_3 layer, which is known to have insulating properties [37–39]. To the authors knowledge there are no literature values for thermally grown Al_2O_3 at 600 °C. Using literature values for pure bulk Al_2O_3 [40] the expected ASR value for ~50 nm Al_2O_3 is several orders of magnitude higher than the measured value. However, this difference is expected because the thermally grown Al-rich oxide formed on Kanthal EF101 cannot be compared to a high purity sintered Al_2O_3 sample.

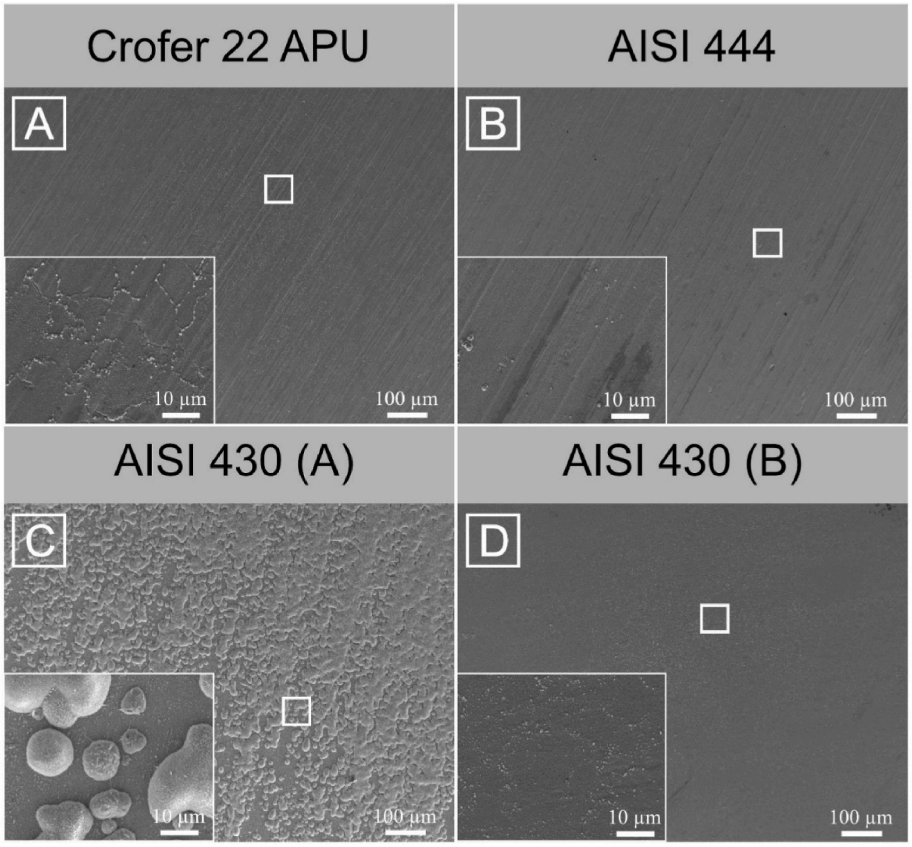

Fig. 4. Top-view SEM micrographs of selected steels exposed under the single-atmosphere condition (air + 3% H_2O) at 600 °C for 500 h. The insets show higher-magnification images of the regions indicated by boxes.

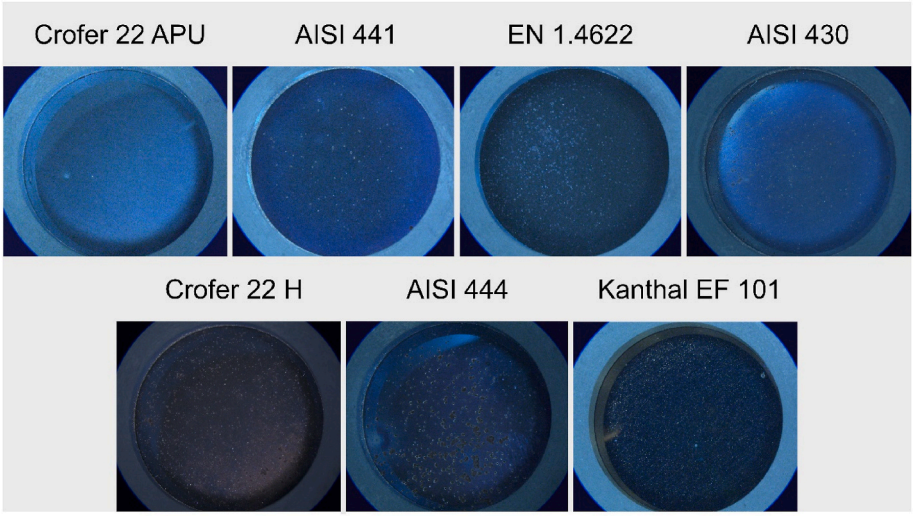

Fig. 5. Photographs of the **air-facing** sides of selected steels exposed to dual-atmosphere conditions (Ar-5% H_2 + 3% H_2O//Air + 3% H_2O) at 600 °C for 500 h. Batch A was used for Crofer 22 APU and Crofer 22 H.

3.1.4. Surface analysis

Fig. 4 shows the top-view SEM micrographs of selected steels exposed under the single-atmosphere condition (air + 3% water vapour). Crofer 22 APU and AISI 444 exhibit a protective oxide scale after 500 h of exposure. XRD analysis (not shown) confirmed the presence of a corundum and spinel phase, which is in line with previous observations regarding the formation of Cr_2O_3 and $(Cr,Mn)_3O_4$ [41]. AISI 430 (A) exhibits the presence of an Fe-rich oxide scale covering almost all of the sample surface. Following pre-oxidisation at 800 °C for 20 min, AISI 430 (B) shows a protective behaviour with a duplex scale of Cr_2O_3/$(Cr, Mn)_3O_4$ and no evidence of breakaway oxidation.

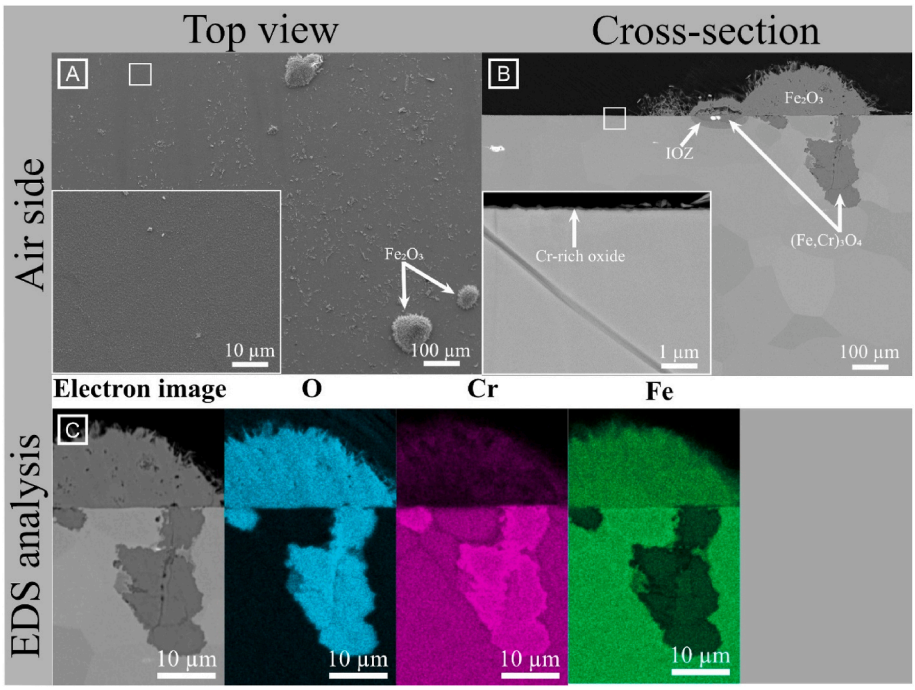

Fig. 6. SEM micrographs of Crofer 22 APU (batch A) representing: a) top-view of the air-side of the exposed sample; b) cross-section of the air-side; c) EDS analysis of the Fe-rich oxide nodule on the Crofer 22 APU uncoated sample that was pre-oxidised for 20 min at 800 °C and exposed to the dual-atmosphere conditions (Ar-5% H_2 + 3% H_2O//Air + 3% H_2O) for 500 h at 600 °C. Insets: Higher-magnification images of selected scale regions.

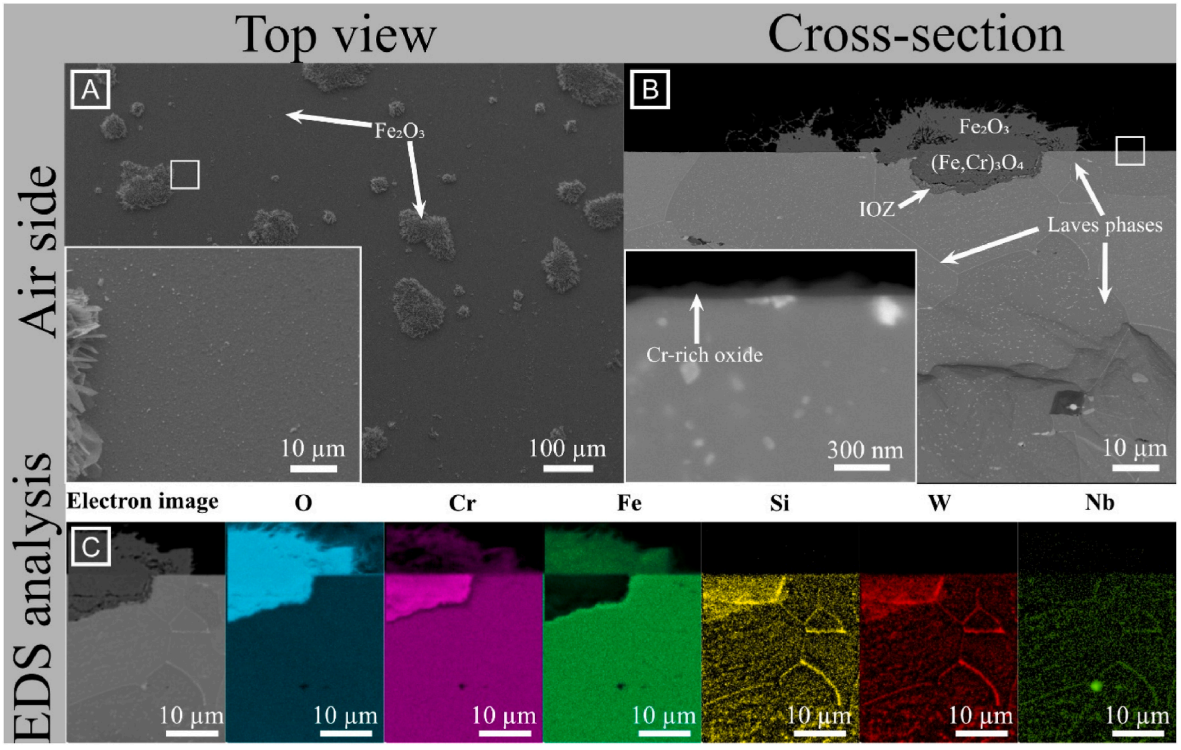

Fig. 7. SEM micrographs of Crofer 22 H (batch A) representing: a) top-view of the air-side of the exposed sample; b) cross-section of the air-side; c) EDS analysis of the Fe-rich oxide nodule on the Crofer 22 H uncoated sample that was pre-oxidised for 20 min at 800 °C and exposed to the dual-atmosphere environment (Ar-5% H_2 + 3% H_2O//Air + 3% H_2O) for 500 h at 600 °C. Inset: Higher-magnification image of selected scale regions.

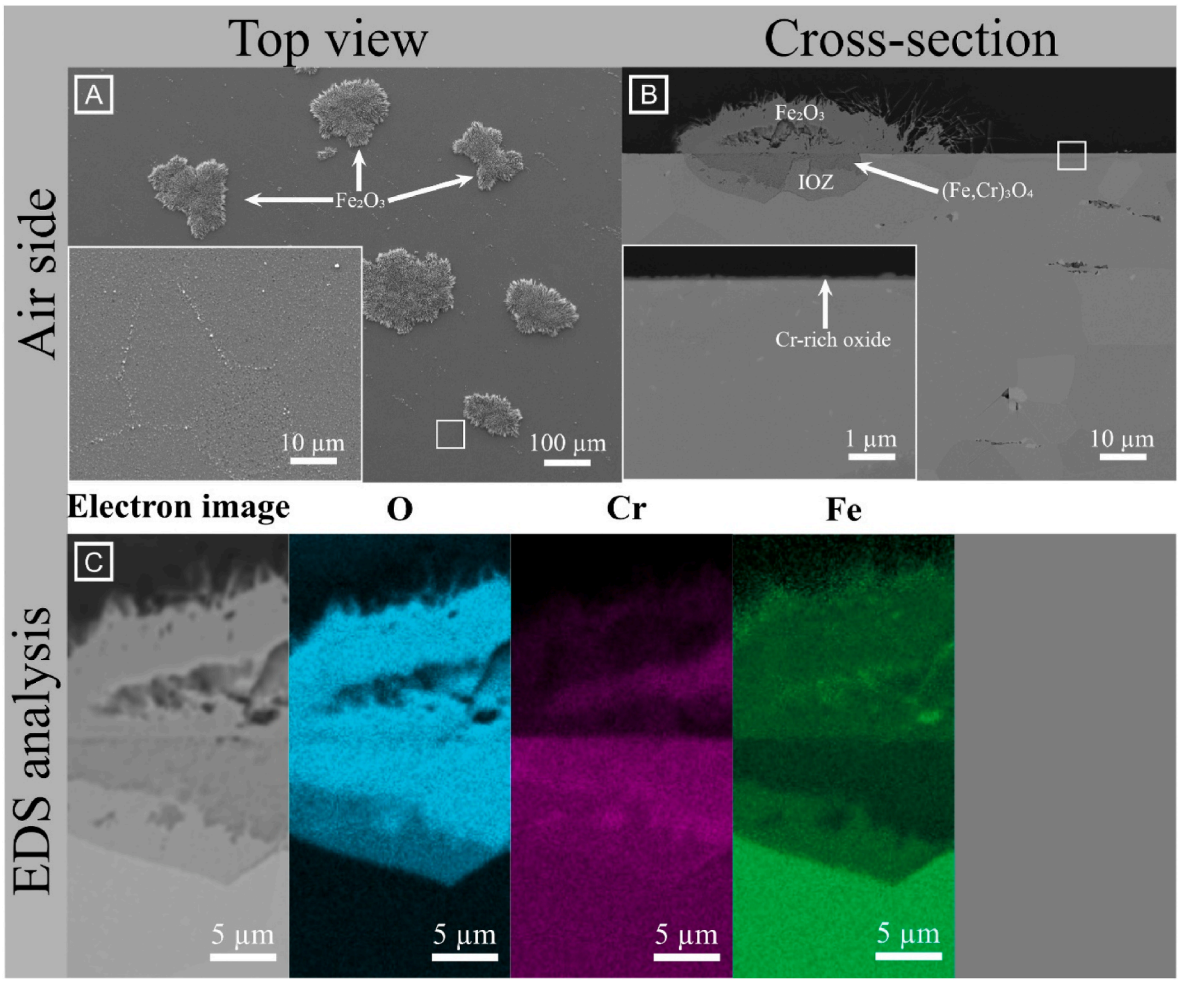

Fig. 8. SEM micrographs of AISI 441 representing: a) top-view of the air-side of the exposed sample; b) cross-section of the air-side; c) EDS analysis of the Fe-rich oxide nodule on the AISI 441 uncoated sample that was pre-oxidised for 20 min at 800 °C and exposed to the dual-atmosphere environment (Ar-5% H_2 + 3% H_2O// Air + 3% H_2O) for 500 h at 600 °C. Inset: Higher-magnification image of selected scale regions.

4. Results

4.1. (Dual-atmosphere condition)

4.1.1. Visual inspection

Fig. 5 shows the air-sides of the different pre-oxidised (for 20 min at 800 °C) steels after exposure for 500 h at 600°Cunder dual-atmosphere conditions. All the samples are covered with a thin base oxide, together with varying amounts of thick Fe oxide. This is in sharp contrast to the images acquired for samples exposed to the single-atmosphere condition, whereby all the samples (except the non-pre-oxidised AISI 430) exhibit protective behaviour. Crofer 22 APU seems to be the least-affected of the Cr_2O_3-forming steels, while Crofer 22 H and AISI 444 seem to have suffered the most-severe corrosion attacks. Intermediate behaviours were observed for the remaining chromia-formers. The Al_2O_3-forming Kanthal EF 101 shows a protective behaviour after exposure.

4.1.2. Crofer 22 APU

Fig. 6 depicts the oxide scale formed on Crofer 22 APU after exposure at 600 °C for 500 h. Fig. 6a shows the top-view SEM image of the air-side. The sample is largely covered by a Cr-rich layer (<100 nm in thickness), although a few Fe_2O_3 oxide nodules can be seen. The nodules are approximately 100 µm in diameter. The cross-section of the air-side surface (see Fig. 6b) reveals a nodule composed of Fe_2O_3 on top, and underneath a (Fe, Cr)$_3O_4$ spinel can be observed (confirmed by EDS mapping, see Fig. 6c), followed by an Internal Oxidation Zone (IOZ). This morphology, which has also been observed in previous studies [9,13,42,43], is characteristic of breakaway oxidation behaviour.

4.1.3. Crofer 22 H

The SEM micrographs and EDS analysis of Crofer 22 H exposed for 500 h at 600 °C under dual-atmosphere conditions (Ar-5% H_2 + 3% H_2O//Air + 3% H_2O) are shown in Fig. 7. Top-view images of the air-side of the sample (see Fig. 7a) show the presence of Fe_2O_3 nodules with average diameters of approximately 50–60 µm. The remaining sample surface appears to be covered by a thin Cr-rich layer (<100 nm in thickness). Fig. 6b shows the cross-section of a nodule that is composed of Fe_2O_3 on top (roughly 10 µm in thickness) and an $(Fe,Cr)_3O_4$ spinel underneath (approximately 10 µm in thickness). A small IOZ can be observed. A significant amount of Laves phases, believed to be composed of $(Fe,Cr,Si)_2(Nb,W)$ [44], can be seen along the grain boundaries and within the grains (see Fig. 7b and c).

4.1.4. AISI 441

SEM micrographs of the surface of AISI 441 exposed under dual-atmosphere conditions (Ar-5% H_2 + 3% H_2O//Air + 3% H_2O) are shown in Fig. 8. The top-view image of the air-side of the sample (see Fig. 8a) depicts the presence of large Fe_2O_3 nodules, which are roughly 100 µm-thick on average). A protective oxide scale is evident between the nodules. The cross-section of the air-side (see Fig. 8b) is in accordance with the observations made from Fig. 8a, showing a nodule of

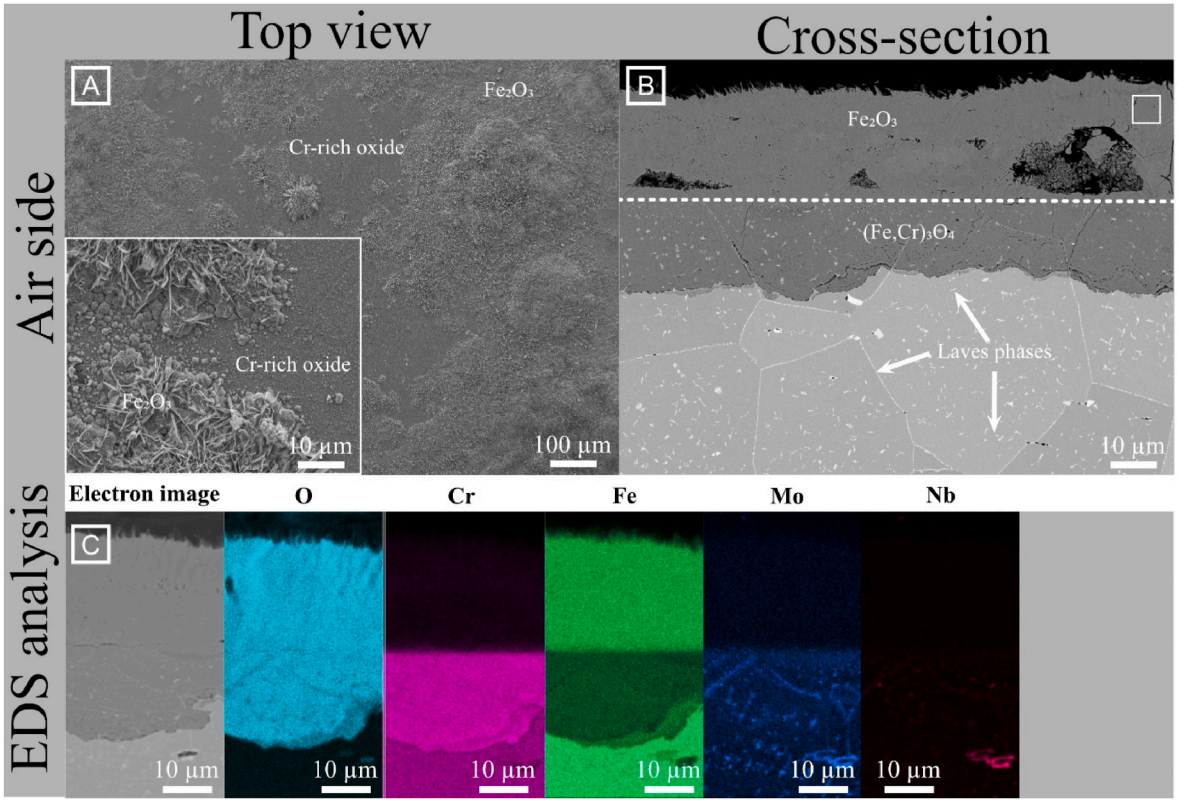

Fig. 9. SEM micrographs of AISI 444 representing: a) top-view of the air-side of the exposed sample; b) cross-section of the air-side; c) EDS analysis of the Fe-rich oxide nodule on the AISI 444 uncoated sample that was pre-oxidised for 20 min at 800 °C and exposed to the dual-atmosphere environment (Ar-5% H_2 + 3% H_2O// Air + 3% H_2O) for 500 h at 600 °C. Insets: Higher-magnification images of selected scale regions.

Fe_2O_3 (~15 μm in thickness) and a thin protective oxide scale that is believed to be Cr-rich (<100 nm in thickness). Beneath the Fe_2O_3 nodule, an (Fe, Cr)$_3O_4$ spinel layer and an IOZ are present.

4.1.5. AISI 444

Fig. 9 depicts the SEM micrographs of AISI 444 after exposure at 600 °C for 500 h under dual-atmosphere conditions (Ar-5% H_2 + 3% H_2O//Air + 3% H_2O). Top-view SEM imaging of the air-side of the sample (Fig. 9a) shows that the sample is mostly covered by a Fe_2O_3 layer. A Cr-rich layer is still visible in a small area of the sample's surface. The cross-section of the air-side of the sample (Fig. 9b) shows a thick Fe-rich layer (~40 μm in thickness) composed of Fe_2O_3 on top (~25 μm in thickness), with an (Fe,Cr)$_3O_4$ spinel (~15 μm in thickness) underneath. EDS analysis confirms the presence of Laves phases, (Fe,Cr, Si)$_2$NbMo, both along the grain boundaries and within the grains (see Fig. 9c).

4.1.6. EN 1.4622

Fig. 10 depicts the SEM micrographs of EN 1.4622 exposed to dual-atmosphere conditions (Ar-5% H_2 + 3% H_2O//Air + 3% H_2O) for 500 h at 600 °C. Fig. 10a shows the presence of Fe_2O_3 nodules, which are roughly 50 μm in thickness on average, on the sample surface, and located between those nodules, there is a protective Cr-rich oxide layer (<100 nm in thickness). The cross-section of the air-side (Fig. 10b) confirms previous observations of an Fe-rich nodule composed of Fe_2O_3 on top (~10 μm in thickness), with an (Fe,Cr)$_3O_4$ (~10 μm in thickness) spinel underneath.

4.1.7. AISI 430

Fig. 11 shows the SEM micrographs of AISI 430 after exposure at 600 °C for 500 h under dual-atmosphere conditions (Ar-5% H_2 + 3% H_2O//Air + 3% H_2O). Fig. 11a represents the top-view SEM image of the air-side of the sample. Fe-rich nodules are visible along the surface, ranging in diameter from 10 μm to 100 μm. In-between these nodules, a protective Cr-rich oxide scale is present. The cross-section of the air-side (Fig. 11b) shows a nodule composed of Fe_2O_3 on top, roughly 10 μm in thickness, and an (Fe,Cr)$_3O_4$ spinel underneath (~10 μm in thickness) that is encapsulated by a Cr_2O_3 layer (<100 nm in thickness). A small IOZ is observed next to the (Fe,Cr)$_3O_4$ spinel. The nodule is surrounded by a protective Cr-rich oxide layer, which is mainly Cr_2O_3. A similar morphology was observed in previous studies [14,45] during dual-atmosphere experiments conducted at 800 °C.

4.1.8. Kanthal EF101

Fig. 12 shows the SEM micrographs of the Kanthal EF101 sample exposed to the dual-atmosphere conditions. The top-view of the air-side (Fig. 12a) depicts a mostly homogeneous, protective Al_2O_3 scale covering the sample. Scarce and relatively small (~10 μm in diameter) Fe-rich nodules are visible on the surface, in addition to some ZrO_2 oxide nodules. Similar ZrO_2 nodules were previously observed by *Sand* et al. [46]. Fig. 12b depicts a cross-section of the air-side oxide scale and the steel that lies underneath. ZrO_2 nodules can be observed on top of the sample and within the bulk. A thin Al_2O_3 oxide layer (<100 nm in thickness) covers the sample. The EDS analysis (Fig. 12c) shows the presence of a somewhat thicker Al_2O_3 layer beneath the ZrO_2 nodules.

4.1.9. Influence of the Laves phases

The comparison of the Cr_2O_3-forming steels indicated a negative influence of the presence of Laves phases, as manifested in the relatively poor performances of Crofer 22 H and AISI 444, which contain the most Laves phase precipitates. To confirm this hypothesis and exclude batch-to-batch variations, three batches of Crofer 22 APU and three batches of Crofer 22 H were selected (Fig. 13) for investigation. The variation in chemical composition between these batches is small (see Table II), and

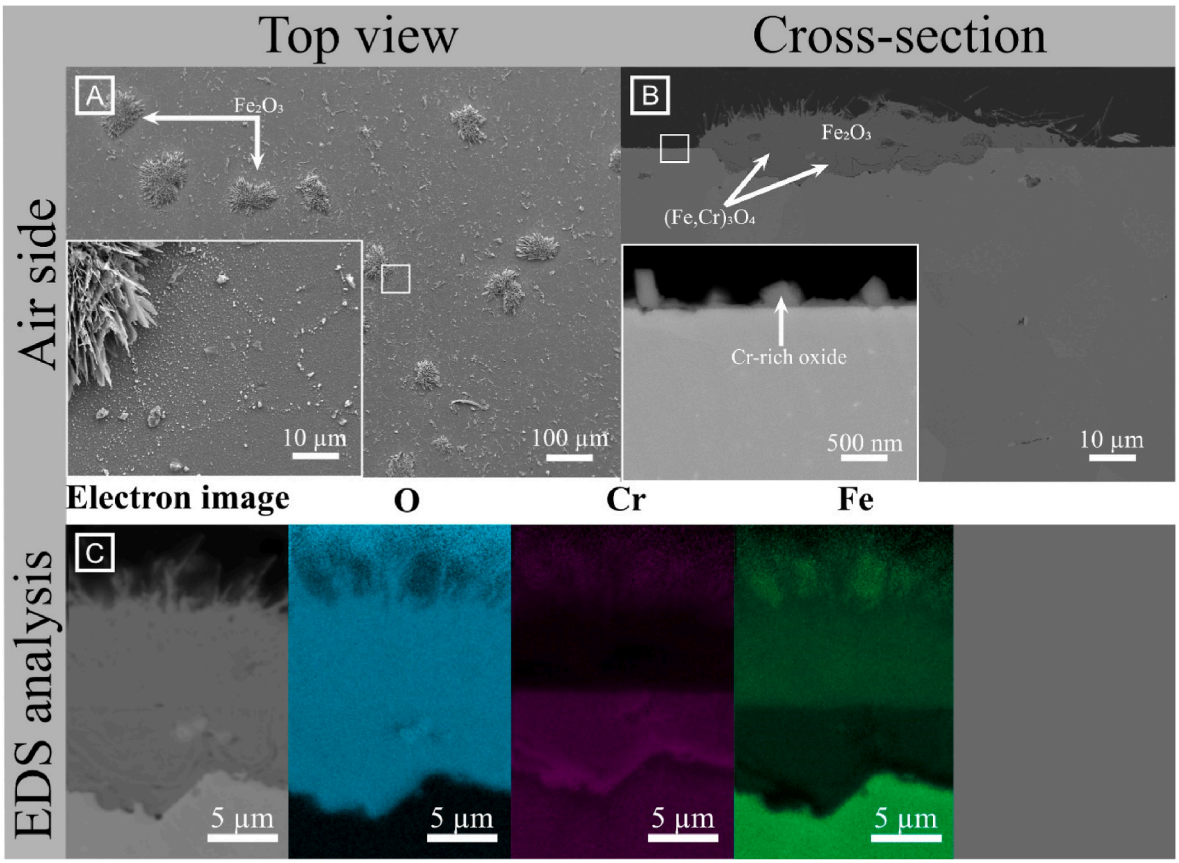

Fig. 10. SEM micrographs of EN 1.4622 representing: a) top-view of the air-side of the exposed sample; b) cross-section of the air-side; c) EDS analysis of the Fe-rich oxide nodule on the EN 1.4622 uncoated sample that was pre-oxidised for 20 min at 800 °C and exposed to the dual-atmosphere environment (Ar-5% H_2 + 3% H_2O// Air + 3% H_2O) for 500 h at 600 °C. Insets: Higher-magnification images of selected scale regions.

the main differences between Crofer 22 APU and Crofer 22 H are the Laves phase-forming elements, such as W, Nb and Si. All the samples were exposed to dual-atmosphere conditions (Ar-5% H_2 + 3% H_2O//Air + 3% H_2O) at 600 °C for 336 h. In the light optical microscopy analysis, the three different batches of Crofer 22 APU (Fig. 13a) appear to be similar. Crofer 22 APU (batches B and C) seem to have slightly more Fe-rich nodules localised to the edge of the sample. This is attributed to an edge effect that probably originates from the sample clamping, which induced some cracking of the oxide scale formed during pre-oxidation, thereby accelerating the corrosion locally. Overall, all three samples appear to be protective after 336 h of exposure, regardless of their batch composition. The three different batches of Crofer 22 H (Fig. 13b) exhibit more-severe corrosion on the air-side than do the Crofer 22 APU samples.

Cross-sections of the fuel side oxide scales were investigated by SEM and can be found in supplemental information S1. Due to the pre-oxidation all fuel-side oxide scales remained thin and protective (<100 nm).

5. Discussion

5.1. (Single-atmosphere condition)

5.1.1. Cr(VI) evaporation

The Cr_2O_3-forming steels, with the exception of the non-pre-oxidised AISI 430, show similar levels of Cr(VI) evaporation, despite their different chemical compositions. The slight variation in Cr(VI) evaporation observed between the different Cr_2O_3-forming steels is assumed to be linked to the Cr concentration in the outermost layer. It has been shown previously that at lower temperatures, such as 600 °C, more Fe is incorporated into the Cr_2O_3 layer than at higher temperatures [47]. Furthermore, it is presently unknown as to whether the outer spinel layer is continuous at 600 °C, and these factors are expected to cause the observed variations.

The previously published Cr(VI) evaporation rates measured at 650 °C are approximately 3-fold higher than those observed in the present study [48,49]. This surprisingly large discrepancy may be attributable to the lower purity level of the Cr_2O_3 layer. AISI 444 has a lower Cr(VI) evaporation than most of the Cr_2O_3-forming steels; the reason for this is presently unknown. AISI 430 (A) displays an approximately 10-fold lower Cr(VI) evaporation level after 500 h of exposure (0.0018 mg cm^{-2}) compared to the other Cr_2O_3-forming steels. This low value is due to breakaway oxidation (see Fig. 4), which leads to the formation of Fe oxide due to the breakdown of the protective chromia layer [50]. To confirm this hypothesis, a set of samples was pre-oxidised for 20 min at 800 °C, so as to form a protective Cr_2O_3 layer, and then exposed at 600 °C under single-atmosphere conditions (air + 3% H_2O) for 3 weeks. The samples exhibit a much higher Cr(VI) evaporation (~0.021 mg cm^{-2}) after 500 h of exposure, which is very similar to that of the other Cr_2O_3-forming steels. AISI 430 (B) exhibits the highest Cr (VI) vaporisation value, which supports the hypothesis that the chromia layer formed at higher temperature (during pre-oxidation) has a higher level of purity (i.e., contains fewer impurities, such as Fe) than those formed at lower temperatures. Kanthal EF 101 exhibits the lowest level of Cr(VI) evaporation (0.00095 mg cm^{-2} after 500 h). This accords with the previous results from *Sand* et al. [46] and *Reddy* et al. [49]. FeCrAl steels are known to form transient alumina layers at lower temperatures [34,35]. *Israelsson* et al. [51] studied similar steel grades by AES and found very low amounts of Cr and Fe in the scale. In addition, Kanthal EF 101 contains 1.25 wt% Si and previous work [52,53] proposed a

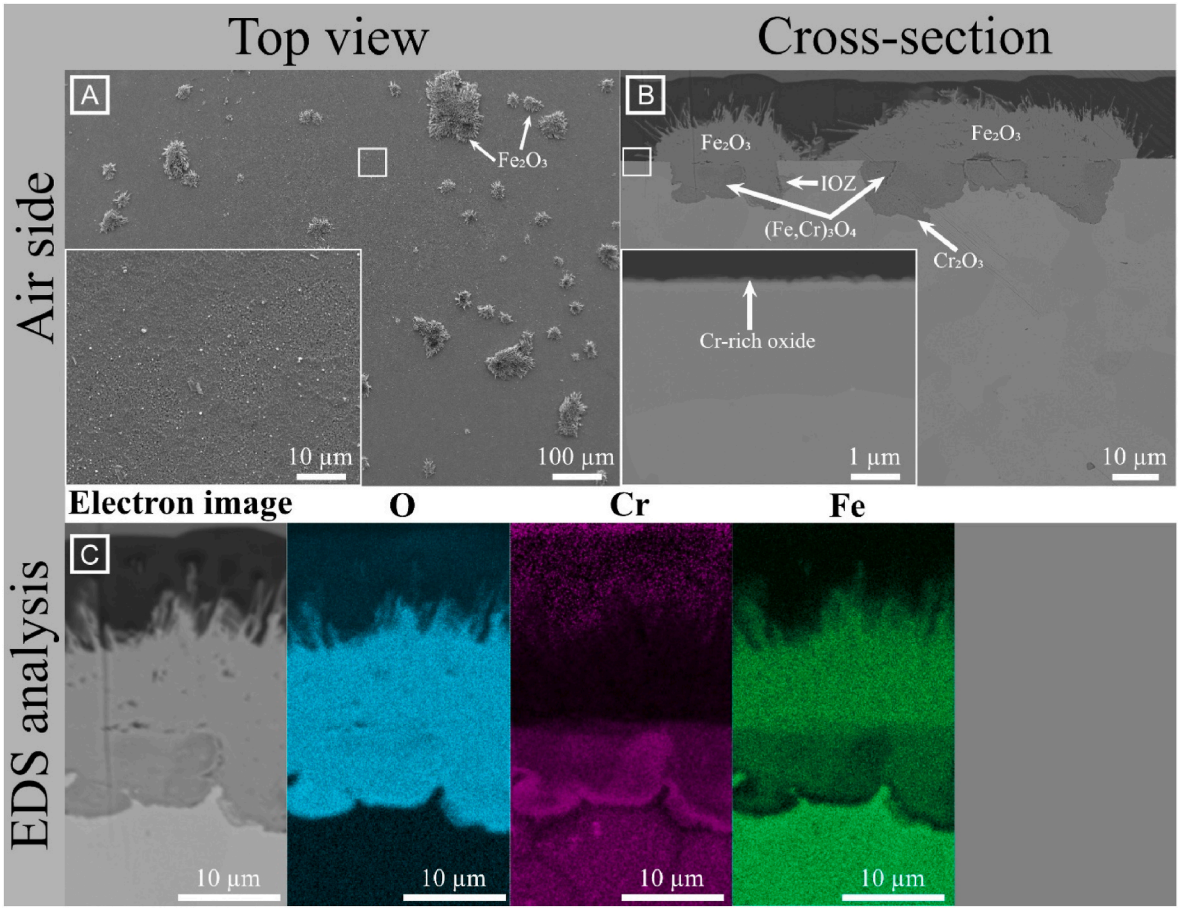

Fig. 11. SEM micrographs of AISI 430 representing: a) top-view of the air-side of the exposed sample; b) cross-section of the air-side; c) EDS analysis of the Fe-rich oxide nodule on the AISI 430 uncoated sample that was pre-oxidised for 20 min at 800 °C and exposed to the dual-atmosphere environment (Ar-5% H_2 + 3% H_2O// Air + 3% H_2O) for 500 h at 600 °C. Insets: Higher-magnification images of selected scale regions.

beneficial of Si on reducing the Cr(VI) evaporation. This results in a drastic reduction of Cr(VI) evaporation compared to the other steels in the study which contain low levels of Al and Si.

5.1.2. Gravimetric measurements

Overall, the net mass gain values of all of the exposed materials, with the exception of AISI 430 (A), are very low (±0.01 mg cm^{-2}). Crofer 22 APU, Crofer 22 H and AISI 441 exhibit slightly negative net mass gains after 500 h of exposure. However, when compensation is made for the mass loss caused by the Cr(VI) evaporation, they show positive gross mass gains. Crofer 22 APU has a slightly higher gross mass gain than Crofer 22 H. *Sachitanand* et al. [54] have reported a similar observation for exposures at high temperatures (850 °C). In the present study, AISI 441 exhibits a mass loss after 500h of exposure of roughly −0.003 mg cm^{-2}, which accords with the previous results of *Reddy* et al. [49]. The higher mass loss seen for Crofer 22 H, followed by Crofer 22 APU and AISI 441, can be explained by the interplay between the oxidation rate and Cr(VI) evaporation. Crofer 22 H has a slower oxidation rate and lower Cr(VI) vaporisation than Crofer 22 APU and AISI 441. Previous work [49] found a similar trend at 650 °C. AISI 430 exhibits two different behaviours. The as-received AISI 430 (A) shows a two orders of magnitude higher net mass gain and an almost equivalent gross mass gain. The fast-growing, Fe-rich oxide that covers the entire surface effectively lowers the level of Cr(VI) evaporation (Fig. 4c).

The reason for the non-protective behaviour of AISI 430 is related to low Cr content leading to faster breakaway oxidation. *Niewolak* et al. [55] tested AISI 430 at 600 °C and found a protective behaviour. The reason for this discrepancy is attributed to the fact that in the present study, a flow of 6000 sml•min^{-1} + 3 % H_2O was used. This results in a higher Cr(VI) evaporation i.e. harsher conditions, compared to stagnant lab air used by *Niewolak* et al. The effect of flow rate was previously showed by *Asteman* et al. [56].

The net mass gain of pre-oxidised AISI 430 (B) is representative of a protective oxide scale (Fig. 4d), so a lower mass gain, of approximately 0.005 mg cm^{-2} after 500 h of exposure, is observed, which is similar to that of AISI 441. Pre-oxidised AISI 430 (B) exhibits the highest gross mass gain of all the steels, with the exception of AISI 430 (A), which reflects a combination of a positive net mass gain and the highest recorded Cr(VI) evaporation (see Fig. 1). Kanthal EF 101 shows similar net and gross mass gains, due to its low level of Cr(VI) evaporation. Alumina is known to be a very stable oxide, and a thin layer is sufficient to reduce drastically the level of Cr(VI) evaporation (see Fig. 1), as compared to Cr_2O_3-forming steels [57,58].

6. Discussion

6.1. (Dual-atmosphere condition)

The results of the present study show that the Cr_2O_3-forming steels (except for AISI 430) behave similarly and remain protective under single-atmosphere conditions (air + 3% H_2O). However, some of these steels undergo severe corrosion when exposed to dual-atmosphere conditions. This is in line with previous observations that the dual-atmosphere effect has greatest severity at around 600 °C [9,10,13]. Previous works conducted by *Goebel* et al. [24] and *Alnegren* et al. [10] have underlined the importance of the pre-oxidation step. *Goebel* et al.

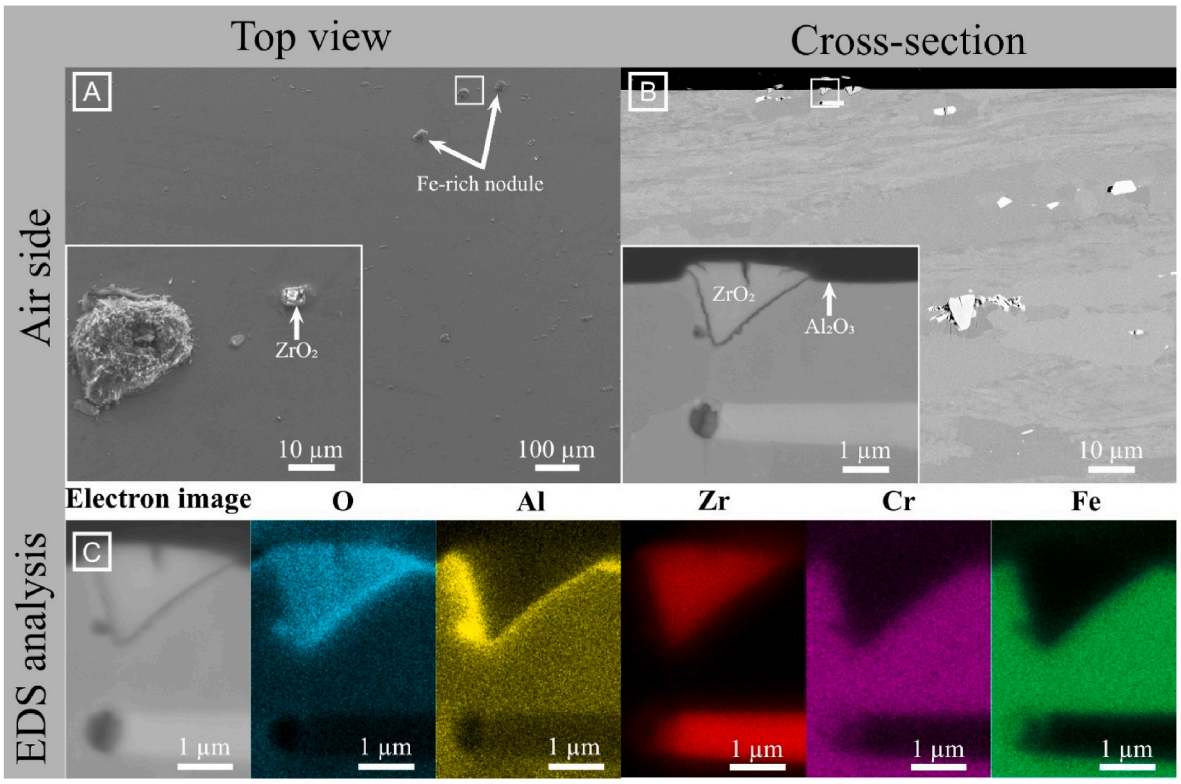

Fig. 12. SEM micrographs of Kanthal EF 101 representing: a) top-view of the air-side of the exposed sample; b) cross-section of the air-side; c) EDS analysis of the RE oxide nodule on the Kanthal EF101 uncoated sample that was pre-oxidised for 20 min at 800 °C and exposed to the dual-atmosphere environment (Ar-5% H_2 + 3% H_2O//Air + 3% H_2O) for 500 h at 600 °C. Insets: Higher-magnification images of selected scale regions.

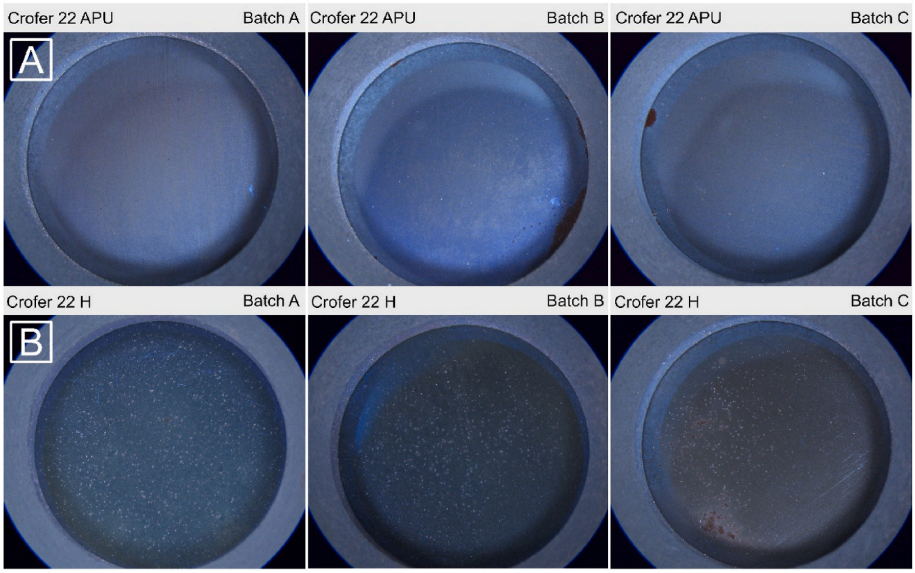

Fig. 13. Optical microscopy top-view images of the air-sides of three different batches of Crofer 22 APU and Crofer 22 H, exposed for 336 h at 600 °C under dual-atmosphere conditions (Ar-5% H_2 + 3% H_2O//Air + 3% H_2O).

[24] have shown that the duration of the pre-oxidation process correlates directly with the period of time for which the sample withstands the dual-atmosphere effect at 600 °C. Different potential mechanisms have been proposed in the literature regarding the dual-atmosphere effect [15,19,59], and they were recently put to the test by *Gunduz* et al. [13]. They have proposed that hydrogen reduces Cr diffusion at the grain boundaries, which promotes the formation of the non-protective, Fe-rich oxide.

For the dual-atmosphere experiments in the present work, all the steels were pre-oxidised for 20 min because non-pre-oxidised steels are expected to form non-protective, Fe-rich oxide scales almost instantaneously [24]. Nevertheless, all the steels (except for Kanthal EF 101) showed non-protective behaviours and suffered from different degrees of breakaway corrosion [58,60]. However, substantial differences in the progress of breakaway corrosion were observed, which will be discussed in more detail. Crofer 22 APU seems to show the best resistance to the

dual-atmosphere effect (see Fig. 6), although some non-protective, Fe-oxide nodules can be found. This behaviour can be linked to a higher concentration of Cr (see Table I), which helps to maintain a protective chromia scale. Furthermore, the steel contains 0.9 wt% lanthanum (La), which is a reactive element (RE). REs are well-known to promote selective oxidation and scale adhesion [7]. In this case, the selective oxidation of Cr to form a protective Cr_2O_3 layer is promoted. Whether La promotes earlier or purer Cr_2O_3 formation or whether it plays a role in maintaining a protective oxide scale at 600 °C, is not well understood. *Kurokawa* et al. [25] have demonstrated that hydrogen permeation through a chromia layer is about four orders of magnitude lower than for an FeCr steel. Therefore, it is possible that the earlier/purer Cr_2O_3 scale on the H_2/H_2O side plays a decisive role here in reducing the ingress of hydrogen. Crofer 22 H shows more-severe corrosion (see Fig. 7), despite having similar amounts of Cr and La (see Table I). The main difference is that the presence of Si (~0.35 wt%), Nb (~0.49 wt%) and W (~1.94 wt%) leads to the formation of a large amount of Laves phases (approximately 7% phase fraction) within the grains and along the steel grain boundaries [61]. While AISI 441 also shows some signs of breakaway corrosion, it performs better than Crofer 22 H despite its lower Cr content. This somewhat surprising finding can be attributed to a smaller phase fraction of Laves phase precipitates (approximately 5% phase fraction), as compared to Crofer 22 H. EN 1.4622 exhibits milder corrosion (see Fig. 10) than Crofer 22 H and AISI 444 but shows more-severe corrosion compared to Crofer 22 APU. AISI 444 seems to suffer from equally severe or more-severe breakaway oxidation as Crofer 22 H (see Fig. 9). While AISI 444 has a somewhat smaller phase fraction of Laves phase (5%), Crofer 22 H benefits from a higher concentration of Cr and the presence of La (~0.7 wt%). AISI 430 suffers a milder corrosion than AISI 444 or Crofer 22 H, despite having a much lower Cr content (see Fig. 11). It is hypothesised that is because AISI 430 does not contain Laves phases. To test this hypothesis, three batches of Crofer 22 APU and Crofer 22 H were exposed to dual-atmosphere conditions for 2 weeks (see Fig. 13). As stated previously, Crofer 22 H forms a high amount of Laves phases, while Crofer 22 APU is free of them. After 336 h of exposure, Crofer 22 H shows more-severe corrosion than Crofer 22 APU. This observation is valid for all three batches. The Laves phases precipitate predominantly at the grain boundaries. In the cases of Crofer 22 H and AISI 444, this might provide an almost continuous network throughout the entire thickness of the sample. *Ponsoni* et al. [62] have described a wide range of Laves phases and have suggested that the Fe_2Nb-type Laves phase can absorb hydrogen. Therefore, it is speculated that the Laves phase precipitates provide easy pathways for hydrogen diffusion through the metal, thereby enhancing the dual-atmosphere-induced corrosion.

An alternative explanation for the poor performance of Crofer 22 H (22% Cr, 7% Laves phase) and the surprisingly strong behaviour of AISI 430 (16% Cr, no Laves phase) is based on differences in grain size. Crofer 22 H exhibits the largest grain size, roughly 32 μm in diameter (see Table III). In contrast, AISI 430 has the smallest grain size (~9 μm in diameter) and exhibits a more-protective behaviour despite having a lower Cr content than either Crofer 22 H or AISI 444. A smaller grain size facilitates more-efficient diffusivity pathways for Cr, and this is expected to be beneficial for sustaining a protective chromia scale on the sample surface. A comparison of AISI 444 and AISI 441 shows that the former is much more-susceptible to dual-atmosphere corrosion. Both steels have similar grain sizes and similar Cr contents, while AISI 444 has an approximately 5-fold higher fraction of Laves phase precipitates, which supports the hypothesis regarding the Laves phase effect.

Kanthal EF 101 stands out in this work, given that the main oxide formed after exposure is Al_2O_3. During dual-atmosphere exposures, the Kanthal EF 101 sample shows very little corrosion, which is attributed to the excellent hydrogen-barrier properties of alumina [63]. The SEM analysis shows the presence of a somewhat thicker Al_2O_3 layer beneath the RE-containing nodules. This agrees with the previously reported results of *Young* et al. [64], in which they demonstrate rapid oxygen transport through the RE particles themselves *Mortazavi* et al. [65] have demonstrated that an RE-doped alumina scale is predominantly inward-growing, promoting scale adhesion by avoiding the porous scale/metal interface that is typical of outward-growing oxide scales. They also observed a thicker Al_2O_3 scale under the RE particles.

7. Conclusion

This work explores the oxidation behaviours of different grades of ferritic stainless steels that are being considered for SOFC applications under single- and dual-atmosphere conditions. In summary, all the materials, with the exception of the non-pre-oxidised AISI 430, perform well in the single-atmosphere experiments. The non-protective behaviour of AISI 430 can be changed with a short pre-oxidation step. The Cr_2O_3-forming steels exhibit small variations in oxidation kinetics and Cr(VI) evaporation levels. These experiments suggest that there are no substantial differences in the applicability of the steels for IT-SOFC applications. However, when exposed to dual-atmosphere conditions, all the Cr_2O_3-forming steels suffer to a certain extent from breakaway corrosion, which is attributed to the low exposure temperature, which impedes Cr diffusion. Steels with a large phase fraction of Laves phase precipitates seem to be more-prone to dual-atmosphere corrosion. Kanthal EF 101 performs excellently under both single- and dual-atmosphere conditions. However, the poor conductivity of alumina makes it difficult to use for IT-SOFC interconnect applications. In contrast, steels that formed protective Cr_2O_3 scales showed consistently low ASR values.

CRediT authorship contribution statement

Matthieu Tomas: Conceptualization, Investigation, Writing – original draft, Writing – review & editing. **Jan-Erik Svensson:** Conceptualization, Funding acquisition, Supervision, Writing – review & editing. **Jan Froitzheim:** Conceptualization, Funding acquisition, Project administration, Supervision, Writing – review & editing.

Declaration of competing interest

The authors declare that they have no known competing financial interests or personal relationships that could have appeared to influence the work reported in this paper.

Acknowledgements

This work was conducted at the Swedish High Temperature Corrosion Centre (HTC) at Chalmers University of Technology. This work was performed in part at the Chalmers Material Analysis Laboratory, CMAL. The authors are grateful for funding by the Swedish Energy Agency through the FFI program and the strategic innovation program Metalliska Material (VINNOVA grant 2021-01003) a joint program by VINNOVA, Formas, and the Swedish Energy Agency.

Appendix A. Supplementary data

Supplementary data to this article can be found online at https://doi.org/10.1016/j.ijhydene.2024.04.010.

References

[1] Brett DJ, Atkinson A, Brandon NP, Skinner SJ. Intermediate temperature solid oxide fuel cells. Chem Soc Rev 2008;37:1568–78.
[2] Oruç Ç, Altındal A. Structural and dielectric properties of CuO nanoparticles. Ceram Int 2017;43:10708–14.
[3] Horita T, Xiong YP, Yoshinaga M, Kishimoto H, Yamaji K, Brito ME, et al. Accelerated degradation of SOFC cathodes by Cr Vapors. SOLID OXIDE FUEL CELLS 2009;11(SOFC-XI):2881–8.

[4] Chen S, Jin X, Rong L. Improvement in high temperature oxidation resistance of 9% Cr ferritic–martensitic steel by enhanced diffusion of Mn. Oxid Metals 2016;85:189–203.
[5] Niewolak L, Young D, Hattendorf H, Singheiser L, Quadakkers W. Mechanisms of oxide scale formation on ferritic interconnect steel in simulated low and high pO2 service environments of solid oxide fuel cells. Oxid Metals 2014;82:123–43.
[6] Niewolak L, Wessel E, Singheiser L, Quadakkers W. Potential suitability of ferritic and austenitic steels as interconnect materials for solid oxide fuel cells operating at 600 C. J Power Sources 2010;195:7600–8.
[7] Hou P, Stringer J. The effect of reactive element additions on the selective oxidation, growth and adhesion of chromia scales. Mater Sci Eng 1995;202:1–10.
[8] Hou PY. The reactive element effect–past, present and future. Materials Science Forum. Trans Tech Publ; 2011. p. 39–44.
[9] Alnegren P, Sattari M, Svensson J-E, Froitzheim J. Severe dual atmosphere effect at 600 C for stainless steel 441. J Power Sources 2016;301:170–8.
[10] Alnegren P, Sattari M, Svensson J-E, Froitzheim J. Temperature dependence of corrosion of ferritic stainless steel in dual atmosphere at 600–800 C. J Power Sources 2018;392:129–38.
[11] Ardigo M, Popa I, Combemale L, Chevalier S, Herbst F, Girardon P. Dual atmosphere study of the K41X stainless steel for interconnect application in high temperature water vapour electrolysis. Int J Hydrogen Energy 2015;40:5305–12.
[12] Gannon P, Amendola R. High-temperature, dual-atmosphere corrosion of solid-oxide fuel cell interconnects. J Miner Met Mater Soc 2012;64:1470–6.
[13] Gunduz KO, Chyrkin A, Goebel C, Hansen L, Hjorth O, Svensson J-E, et al. The effect of hydrogen on the breakdown of the protective oxide scale in solid oxide fuel cell interconnects. Corrosion Sci 2021;179:109112.
[14] Yang Z, Walker MS, Singh P, Stevenson JW. Anomalous corrosion behavior of stainless steels under SOFC interconnect exposure conditions. Electrochem Solid State Lett 2003;6:B35.
[15] Yang Z, Walker MS, Singh P, Stevenson JW, Norby T. Oxidation behavior of ferritic stainless steels under SOFC interconnect exposure conditions. J Electrochem Soc 2004;151:B669.
[16] Horita T, Xiong Y, Yamaji K, Sakai N, Yokokawa H. Evaluation of Fe-Cr alloys as interconnects for reduced operation temperature SOFCs. J Electrochem Soc 2003;150:A243.
[17] Gagliani L, Visibile A, Gündüz KÖ, Svensson J-E, Froitzheim J. The influence of humidity content on ferritic stainless steels used in solid oxide fuel cell under dual atmosphere conditions at 600° C. ECS Trans 2021;103:1809.
[18] Nakagawa K, Matsunaga Y, Yanagisawa T. Corrosion behavior of ferritic steels on the air sides of boiler tubes in a steam/air dual environment. Mater A T High Temp 2003;20:67–73.
[19] Rufner J, Gannon P, White P, Deibert M, Teintze S, Smith R, et al. Oxidation behavior of stainless steel 430 and 441 at 800 C in single (air/air) and dual atmosphere (air/hydrogen) exposures. Int J Hydrogen Energy 2008;33:1392–8.
[20] Ardigo-Besnard MR, Popa I, Chevalier S. Impact of pre-oxidation on the reactivity and conductivity in H2–H2O atmosphere of a ferritic stainless steel for high temperature water vapour electrolysis. Int J Hydrogen Energy 2022;47:23508–13.
[21] Reisert M, Aphale AN, Anisur MR, Belko S, Yaginuma M, Shiomi T, et al. Controlled thermal pre-treatment of ZMG232G10® for corrosion mitigation under simulated SOFC interconnect exposure conditions. Int J Hydrogen Energy 2023;48:18420–32.
[22] Amendola R, Gannon P, Ellingwood B, Hoyt K, Piccardo P, Genocchio P. Oxidation behavior of coated and preoxidized ferritic steel in single and dual atmosphere exposures at 800°C. Surf Coating Technol 2012;206:2173–80.
[23] Fontana S, Vuksa M, Chevalier S, Caboche G, Piccardo P. On the effect of surface treatment to improve oxidation resistance and conductivity of metallic interconnects for SOFC in operating conditions. Mater Sci Forum 2008;595–598:753–62.
[24] Goebel C, Alnegren P, Faust R, Svensson J-E, Froitzheim J. The effect of pre-oxidation parameters on the corrosion behavior of AISI 441 in dual atmosphere. Int J Hydrogen Energy 2018;43:14665–74.
[25] Kurokawa H, Oyama Y, Kawamura K, Maruyama T. Hydrogen permeation through Fe-16Cr alloy interconnect in atmosphere simulating SOFC at 1073 K. J Electrochem Soc 2004;151:A1264.
[26] Tomas M, Visibile A, Svensson JE, Froitzheim J. Novel coatings for protecting solid oxide fuel cell interconnects against the dual-atmosphere effect. Int J Hydrogen Energy 2023;48:18405–19.
[27] Alnegren P, Sattari M, Svensson J-E, Froitzheim J. Severe dual atmosphere effect at 600 °C for stainless steel 441. J Power Sources 2016;301:170–8.
[28] Sanchez MG, Oum M, Pandyian S, Majewski A, Troskialina L, Steinberger-Wilckens R. Scored 2: 0-Steel coatings for reducing degradation. Belgium: Report University of Birmingham; 2017.
[29] Yasuda N, Uehara T, Tanaka S, Yamamura K. Development of A New alloy for SOFC interconnects. Supplemental Proceedings: Materials Processing and Energy Materials 2011;1:439–46.
[30] Froitzheim J, Ravash H, Larsson E, Johansson L-G, Svensson J-E. Investigation of chromium volatilization from FeCr interconnects by a denuder technique. J Electrochem Soc 2010;157:B1295–300.
[31] Froitzheim J, Ravash H, Larsson E, Johansson LG, Svensson JE. Investigation of chromium volatilization from FeCr interconnects by a denuder technique. J Electrochem Soc 2010;157:B1295.
[32] Sachitanand R, Sattari M, Svensson J-E, Froitzheim J. Evaluation of the oxidation and Cr evaporation properties of selected FeCr alloys used as SOFC interconnects. Int J Hydrogen Energy 2013;38:15328–34.
[33] Yatoo MA, Habib F, Malik AH, Qazi MJ, Ahmad S, Ganayee MA, et al. Solid-oxide fuel cells: a critical review of materials for cell components. MRS Communications 2023;13:378–84.
[34] Eklund J, Jönsson B, Persdotter A, Liske J, Svensson J-E, Jonsson T. The influence of silicon on the corrosion properties of FeCrAl model alloys in oxidizing environments at 600 C. Corrosion Sci 2018;144:266–76.
[35] Israelsson N, Hellström K, Svensson J-E, Johansson L-G. KCl-induced corrosion of the FeCrAl alloy Kanthal® AF at 600° C and the effect of H 2 O. Oxid Metals 2015;83:1–27.
[36] Windisch HF. Improved oxidation resistance and reduced Cr vaporization from thin-film coated Solid oxide fuel Cell interconnects. 2017.
[37] Schemmel R, Philipp L, Stringer J, Gordon R. Electrical properties of a polycrystalline alumina sample. Hanford Engineering Development Lab. 1972 Richland, WA (United States).
[38] Cohen J. Electrical conductivity of alumina. J Am Ceram Soc 1959;38:441–6.
[39] Arizumi T, Tani S. On the electrical conductivity of alumina. J Phys Soc Jpn 1950;5:442–7.
[40] Özkan OT, Moulson AJ. The electrical conductivity of single-crystal and polycrystalline aluminium oxide. J Phys Appl Phys 1970;3:983.
[41] Falk-Windisch H, Svensson JE, Froitzheim J. The effect of temperature on chromium vaporization and oxide scale growth on interconnect steels for Solid Oxide Fuel Cells. J Power Sources 2015;287:25–35.
[42] Stygar M, Matsuda K, Lee S, Brylewski T. Corrosion behavior of crofer 22APU for metallic interconnects in single and dual atmosphere exposures at 1073 K. Acta Phys Pol, A 2017;131:1394–8.
[43] Reddy MJ, Visibile A, Svensson J-E, Froitzheim J. Investigation of coated FeCr steels for application as solid oxide fuel cell interconnects under dual-atmosphere conditions. Int J Hydrogen Energy 2023.
[44] Hsiao Z-W, Kuhn B, Chen D, Singheiser L, Kuo J-C, Lin D-Y. Characterization of Laves phase in Crofer 22 H stainless steel. Micron 2015;74:59–64.
[45] Yang Z, Xia G-G, Walker MS, Wang C-M, Stevenson JW, Singh P. High temperature oxidation/corrosion behavior of metals and alloys under a hydrogen gradient. Int J Hydrogen Energy 2007;32:3770–7.
[46] Sand T, Edgren A, Geers C, Asokan V, Eklund J, Helander T, et al. Exploring the effect of silicon on the high temperature corrosion of lean FeCrAl alloys in humid air. Oxid Metals 2021;95:221–38.
[47] Segerdahl K, Svensson J-E, Johansson L-G. Protective and nonprotective behavior of 11% Cr steel in O 2+ H 2 O environment at 450-700° C. J Electrochem Soc 2004;151:B394.
[48] Tomas M, Asokan V, Puranen J, Svensson JE, Froitzheim J. Efficiencies of cobalt- and copper-based coatings applied by different deposition processes for applications in intermediate-temperature solid oxide fuel cells. Int J Hydrogen Energy 2022;47:32628–40.
[49] Reddy MJ, Svensson J-E, Froitzheim J. Evaluating candidate materials for balance of plant components in SOFC: oxidation and Cr evaporation properties. Corrosion Sci 2021;190:109671.
[50] Evans H, Donaldson A, Gilmour T. Mechanisms of breakaway oxidation and application to a chromia-forming steel. Oxid Metals 1999;52:379–402.
[51] Israelsson N, Hellström K, Svensson JE, Johansson LG. KCl-induced corrosion of the FeCrAl alloy Kanthal®AF at 600 °C and the effect of H2O. Oxid Metals 2015;83:1–27.
[52] Sand T, Edgren A, Geers C, Asokan V, Eklund J, Helander T, et al. Exploring the effect of silicon on the high temperature corrosion of lean FeCrAl alloys in humid air. Oxid Metals 2021;95:221–38.
[53] Eklund J, Jönsson B, Persdotter A, Liske J, Svensson JE, Jonsson T. The influence of silicon on the corrosion properties of FeCrAl model alloys in oxidizing environments at 600 °C. Corrosion Sci 2018;144:266–76.
[54] Sachitanand R, Sattari M, Svensson J-E, Froitzheim J. Evaluation of the oxidation and Cr evaporation properties of selected FeCr alloys used as SOFC interconnects, vol. 38; 2013. p. 15328–34.
[55] Niewolak L, Wessel E, Singheiser L, Quadakkers WJ. Potential suitability of ferritic and austenitic steels as interconnect materials for solid oxide fuel cells operating at 600°C. J Power Sources 2010;195:7600–8.
[56] Asteman H, Svensson JE, Norell M, Johansson LG. Influence of water vapor and flow rate on the high-temperature oxidation of 304L; effect of chromium oxide hydroxide evaporation. Oxid Metals 2000;54:11–26.
[57] Shirasaka H, Shimonosono T, Hirata Y, Sameshima S. Analysis of gas permeability of porous alumina powder compacts. Journal of Asian Ceramic Societies 2013;1:368–73.
[58] Reisert M, Anisur M, Lee L, Aphale A, Hong J, Yaginuma M, et al. Corrosion of chromia-forming and alumina-forming ferritic stainless steels under dual atmosphere exposure conditions. J Electrochem Soc 2021;168:111506.
[59] Essuman E, Meier G, Żurek J, Hänsel M, Quadakkers W. The effect of water vapor on selective oxidation of Fe–Cr alloys. Oxid Metals 2008;69:143–62.
[60] Reisert M, Aphale A, Singh P. Observations on accelerated oxidation of a ferritic stainless steel under dual atmosphere exposure conditions. In: Energy technology. Springer; 2019. p. 273–81. 2019.
[61] Niewolak L, Savenko A, Grüner D, Hattendorf H, Breuer U, Quadakkers WJ. Temperature dependence of laves phase composition in Nb, W and Si-alloyed high chromium ferritic steels for SOFC interconnect applications. J Phase Equilibria Diffus 2015;36:471–84.
[62] Ponsoni JB, Aranda V, Nascimento TdS, Strozi RB, Botta WJ, Zepon G. Design of multicomponent alloys with C14 laves phase structure for hydrogen storage assisted by computational thermodynamic. Acta Mater 2022;240:118317.

[63] Tomas M, Visibile A, Svensson J-E, Froitzheim J. Novel coatings for protecting solid oxide fuel cell interconnects against the dual-atmosphere effect. Int J Hydrogen Energy 2023;48:18405–19.
[64] Young D, Naumenko D, Wessel E, Singheiser L, Quadakkers W. Effect of Zr additions on the oxidation kinetics of FeCrAlY alloys in low and high p O 2 gases. Metall Mater Trans 2011;42:1173–83.
[65] Mortazavi N, Geers C, Esmaily M, Babic V, Sattari M, Lindgren K, et al. Interplay of water and reactive elements in oxidation of alumina-forming alloys. Nat Mater 2018;17:610–7.